March 17, 2004

Annular Dark Field Imaging in a TEM

S. Bals[1], B. Kabius[2], M. Haider[3], V. Radmilovic[1] and C. Kisielowski[1*]

[1]*National Center for Electron Microscopy, Lawrence Berkeley National Laboratory, One Cyclotron Road, Berkeley CA 94720, USA*

[2]*Materials Science Division; Bldg. 212 Argonne National Laboratory 9700 S. Cass Ave. Argonne IL 60439, USA*

[3]*CEOS GmbH, Englerstr. 28, D-69126 Heidelberg, Germany*

Abstract

Annular objective apertures are fabricated for a CM300 transmission electron microscope using a focused ion beam system. A central beam stop in the back focal plane of the objective lens of the microscope blocks all electrons scattered up to a semi-angle of approximately 20 mrad. In this manner, contributions to the image from Bragg scattering are largely reduced and the image contrast is sensitive to the atomic number Z. Experimentally, we find that single atom scattering cross sections measured with this technique are close to Rutherford scattering values. A comparison between this new method and STEM-HAADF shows that both techniques result in qualitatively similar images although the resolution of ADF-TEM is limited by contrast delocalization caused by the spherical aberration of the objective lens. This problem can be overcome by using an aberration corrected microscope.

PACS codes: 61.16.Bg

Keywords: E. Dark Field TEM, E. Z-contrast

Corresponding author: CFKisielowski@lbl.gov (Christian Kisielowski) fax nr: (510) 486-5888

Introduction

Annular objective transmission electron microscope (TEM) apertures have been used in the past for different reasons such as texture determination in crystalline samples (selected-zone dark-field electron microscopy) [1,2] and contrast improvement [1,3].

Annular apertures allow selecting electrons passed through given symmetric zones within the objective lens of the microscope. One can select zones with a large semi-angle (approximately 50 mrad) where electron scattering is dominated by Rutherford scattering [4]. The electron scattering cross sections for this mechanism are proportional to Z^2 (with Z being the atomic number) and thus the recorded signal amplifies chemical differences.

From a practical point of view, imaging using annular objective TEM apertures with a central beam stop is limited by small intensities at high diffraction angles. Exposure times of 5 – 10 seconds can be achieved in a TEM with an acceleration voltage of 150 kV and a Schottky field emitter for electrons scattered through diffraction angles between 20 and 40 mrad. Under such conditions, decent contrast, sensitive to Z, can be obtained in the annular dark field (ADF) images, which will be demonstrated in this study. Furthermore, the electron scattering cross sections for ADF-TEM can be determined and compared to the theoretical values for Rutherford scattering.

Although Z-contrast imaging has been recently carried out in a TEM using hollow-cone illumination [5], the method commonly refers to high angle annular dark field images (HAADF) recorded with a Scanning Transmission Electron Microscope

(STEM). Therefore, special attention will be devoted to the comparison between ADF-TEM using annular objective apertures and HAADF-STEM.

ADF-TEM is a promising technique for electron tomography because the recorded image is a chemically sensitive projection of the crystal structure [6] with the advantage of having a reduced noise which is caused in STEM by the limited beam current of a small electron probe and, in addition, the ADF-TEM signal can be linearized as will be demonstrated in this letter.

Experimental

The annular objective TEM apertures used in this study are fabricated using a focused ion beam (FIB) system (FEI FIB DB Strata 235) that contains both a focused Ga^+ ion beam and a field emission scanning electron column. The aperture geometry is cut from a 10 μm thick Pt foil, attached to a commercially available thin foil gold aperture with a diameter of 2 mm. A secondary electron image of an aperture during fabrication using the FIB is shown in Figure 1.a.

Figure 1.b. shows the aperture in the TEM, acting as a central beam stop in the back focal plane of the objective lens of the microscope. The diameter of the central beam stop is approximately 90 μm. It allows recording electrons scattered beyond a semi-angle of approximately 20 mrad and an outer ring diameter of 180 μm corresponds to a maximum collection angle of 40 mrad for electrons accelerated by 150kV.

The ADF-TEM images have been recorded with a Philips CM300 equipped with a Schottky field emitter and an ultra-twin lens with a spherical aberration coefficient C_s =

0.60 mm. The microscope was operated at 150 kV in order to eliminate transmission of central beam intensity and reduce radiation damage. The HAADF-STEM study was performed using a Tecnai G^2 UTWIN STEM field emission microscope, operated at 200 kV.

Results and discussion

ADF-TEM

Figure 2.a. shows a bright field image (taken at Gaussian defocus) of a CdTe tetrapod (average Z = 50) next to a Au (Z = 79) and a CdTe nanoparticle on an amorphous carbon film. The growth and characterization of the CdTe tetrapods is described in [7]. The tetrapod is imaged looking down the [001] direction of one branch and can be recognized by the darker contrast in the central part of the image. The image is visualized at Gaussian defocus for the carbon film. Since 3 branches of the tetrapod lie in the same plane (on the carbon film) [8] they are also imaged at nearly exact Gaussian defocus. After insertion of the annular objective aperture and defocusing of the objective lens about -2500Å to minimize contrast delocalization [9], the image shown in Figure 2.b is obtained. Intensity profiles are made for both images along the direction indicated by the white line in Figure 2.a. The ADF intensity profile shows a signal to noise (S/N) ratio of approximately 10:1. The ~ 25 nm tall projected central branch of the tetrapod generates a smaller signal than the ~ 5 nm small gold sphere which indicates that the ADF image contrast amplifies chemical differences.

The lattice fringes visible in the ADF images are strongly delocalized. Figure 3.a shows a regular high resolution bright field image of a Au nanoparticle taken at Gaussian defocus. After Fourier filtering the image with a mask equivalent to the annular objective aperture in the TEM (Figure 3b), the Au particle can barely be distinguished from the background. The corresponding ADF image (Figure 3.c) again exhibits strong contrast delocalization. When the same experiment is carried out for a bright field image (Figure 3.d) taken at an underfocus of –2260 Å (which is an experimentally determined optimum defocus value for ADF imaging in this case), the application of the mask in Fourier space yields Figure 3.e. The Au particle is now visible with a better S/N ratio compared to Figure 3.b (cfr. intensity profiles) since a focus of least confusion for the ADF image has been applied (Figure 3.f).

The importance of using the defocus of least confusion can be understood by considering the effect of spherical aberration of the objective lens: electrons scattered to higher angles are focused higher along the optic axis [10]:

(1) $$\Delta z = C_s \theta^2$$

where θ is the semi-angle, C_s the spherical aberration constant, and Δz the distance between the Gaussian focus (focus = 0) and the point along the optic axis where the given diffracted beams are focused. Since C_s = 0.60 mm and θ = 20 mrad an optimal focus of Δz = -2400 Å is calculated in agreement with the optimal ADF defocus values found in our experiments.

Electron scattering cross-section

A GaN wedge has been used to extract electron scattering cross sections. The local sample thickness is determined experimentally from extinction oscillations of the zero beam in a bright field image that are fitted to multi-slice calculations [11]. The local thickness of the GaN wedge can be related to the intensity of the ADF-TEM image from the same area. Figure 4 shows that the ADF signal can be described through an electron scattering process that depends exponentially on sample thickness. The following expression has already been suggested to describe HAADF images:

$$I/I_0=(1-\exp(-N\sigma\rho t)) \quad (2)$$

where $N=N_0/A$ is Avogadro's constant divided by the atomic weight A, σ is a single-atom scattering cross section, ρ is the materials density and t is the local column height (thickness) [12].

A least square fit of the data in Figure 4 with equation (2) gave a value of $4.2\ 10^{-18}$ cm^2 for the electron scattering cross section. The theoretical value for σ_{GaN} derived from the Rutherford cross section value can be calculated to be $\sigma_{GaN} = 2.9\ 10^{-18}$ cm^2, which is in good agreement to the value measured from our ADF-TEM data. Repeating the experiment using a Au wedge, we confirmed that the experimental electron scattering cross section ($\sigma_{Au,exp} = 3.6\ 10^{-17}$ cm^2) exceeds the theoretical Rutherford value ($\sigma_{Au} = 2.1\ 10^{-17}$ cm^2) slightly. A similar result was found for HAADF-STEM images of Au wedges [13]. These results imply that it is possible to linearize and quantify ADF-TEM and HAADF-STEM images.

ADF-TEM vs. HAADF-STEM

Image formation by HAADF-STEM is sensitive to Z since the detector collects electrons scattered through high angles. Furthermore, the technique is incoherent because of the geometry of the detector and contributions of phonon scattering [14]. In ADF-TEM, the illumination is coherent, but again, electrons scattered to high angles are detected, which increases the contribution of incoherent scattering. Despite the fact that the collection angle used in our ADF-TEM technique is too small to exclude all diffraction contrast from the recorded signal, the technique is found to be chemically sensitive as already demonstrated in Figure 2 and discussed in the previous section.

In Figure 5 an ADF-TEM image is compared to a HAADF-STEM image taken from the same area of a multi layer system. A bright field image of the sample is shown in Figure 5.a: the Si substrate is followed by a layer sequence of: SiO_2/Ta/Cu/TiAl (50:50)/(Ba,Sr)TiO_3. The microscope settings in both ADF-TEM and HAADF-STEM are such that electrons scattered through a semi-angle of > 20 mrad are used for imaging.

As can be seen in Figures 5.b (ADF-TEM) and 5.c (HAADF-STEM) both techniques result in qualitatively similar images in which the chemically different layers can clearly be distinguished from each other. However, the resolution of the ADF-TEM image is limited in the present study by the spherical aberration of the objective lens, which causes contrast delocalization. As a consequence the signal of the intensity profiles is broadened. The effect of spherical aberration in ADF-TEM is large since the distortion is proportional to $C_s\theta^3$ and the beams collected by the annular objective apertures are far from the optical axis.

To a certain extend, ADF-TEM images can be corrected for spherical aberration by deconvolution with the correct point spread function, which can be determined by comparison of the (blurred) ADF-TEM image to the HAADF-STEM image [15]. Aberration corrected microscopes will enable a much better resolution for ADF-TEM because contrast delocalization can be reduced to values below the information limit of the instrument. In this case Cc will limit the resolution similar to HAADF-STEM.

Conclusions

We demonstrate that dark field imaging in a TEM using an annular objective aperture generates chemically sensitive images of crystal structures that lack any scanning noise. Aperture design became feasible by the development of focused ion beam technology. Signals can be quantified by extraction of electron scattering cross sections that are close to the values for Rutherford scattering. From comparison between ADF-TEM and HAADF-STEM it is clear that the effect of the spherical aberration of the objective lens in this study is larger for ADF-TEM.

Acknowledgements

We are grateful to Prof. H. Rose for helpful discussions. We thank Prof. A.P. Alivisatos for provision of the CdTe samples. Thanks also to Dr. R. Erni for the STEM results. This work was supported by the Director, Office of Science, Office of Basic Energy Sciences, of the U.S. Departement of Energy under Contract No. DE-AC03-76SF00098. This work was supported by the U.S. Department of Energy, Office of Science, under contract #W-31-109-Eng-38.

References

[1] K. Heinemann and H. Poppa, Appl. Phys. Lett. **20** (1972) 122

[2] M.J. Williamson, D.N. Dunn, R. Hull, S. Kodambaka, I. Petrov, J.E. Greene, Appl. Phys. Lett. **78** (2001) 2223

[3] G. Dupouy, Journal of Electron Microscopy **16** (1967) 5

[4] D.B. Williams and C.B. Carter in Transmission Electron Microscopy, Plenum Press, New York, London 1996 p. 359

[5] U. Kaiser, A. Chuvilin, Microscopy and Microanalysis **9** (2003) 36

[6] P.W. Hawkes in Tomography: Three-dimensional Imaging with the Transmission Electron Microscope, Plenum Press, New York, London 1992

[7] L Manna, D.J. Milliron, A. Meisel, E.C. Scher, A.P. Alivisatos, Nature Materials **2** (2003) 382

[8] C. Kisielowski, S.Bals, C. Nelson, H.Sui, K.H. Downing, Proceedings of International Symposium on the Creation of Novel Nanomaterials, Osaka University, Japan, January 20-22, 2004

[9] H. Lichte, Ultramicroscopy **38** (1991) 13

[10] D.B. Williams and C.B. Carter in Transmission Electron Microscopy, Plenum Press, New York, London 1996 p. 98

[11] C. Kisielowski, Z. Liliental-Weber and S. Nakamura Jpn. J. Appl. Phys. **36** (1997) 6932

[12] R.D. Heidenreich in Fundamentals of Transmission Electron Microscopy, John Wiley & Sons, New York 1964, p. 31

[13] C. Kisielowski, work in progress

[14] P.D. Nellist and S.J. Pennycook Advances in Imaging and Electron Physics **113** (2000) 147

[15] S. Bals and C. Kisielowski, work in progress

Figure captions

Figure 1

a) Secondary electron image of an annular aperture during the fabrication using the FIB system

b) Using a beam stop in the back focal plane of the objective lens, a large part of the Bragg electrons is blocked from imaging.

Figure 2

a) Bright field image of a CdTe tetrapod (one "branch" coming out of the plane) next to a Au and a CdTe nanoparticle. A line scan is made along the direction indicated by the white line.

b) Corresponding ADF-TEM image using a central beam stop in the back focal plane of the objective lens. The line scan shows that the contrast in the image is chemically sensitive.

Figure 3

a) Bright field image of a Au nanoparticle at Gaussian defocus.

b) After Fourier transformation of (a), a mask is applied to simulate the annular objective aperture. Inverse Fourier transformation results in the image shown here, in which the Au particle can barely be distinguished from the background.

c) ADF image corresponding to (a), the signal is very much delocalized.

d) Bright field image of a Au nanoparticle at –2260 Å defocus.

e) Simulation of the annular objective aperture for (d). The Au particle appears sharper for this defocus compared to (b).

f) ADF image corresponding to (d), delocalization of the signal at this defocus setting is less compared to (c).

Figure 4

Dark field intensity vs. sample thickness for a GaN wedge. From this plot the electron scattering cross section can be determined and is found to be in good agreement to the value for Rutherford scattering.

Figure 5

Comparison between an ADF-TEM image (b) and a HAADF-STEM image (c) taken from the same sample. In both techniques, electrons scattered through a semi angle of > 20 mrad are used for imaging. The sample consists of a Si substrate with a multilayer system having the following sequence (right to left):

SiO_2/Ta/Cu/TiAl(50:50)/(Ba,Sr)TiO_3 as shown in the TEM bright-field image (a).

Delocalization of the TEM image causes broadening of the peaks in the intensity profile (made along the directions indicated by white rectangles).

Figures

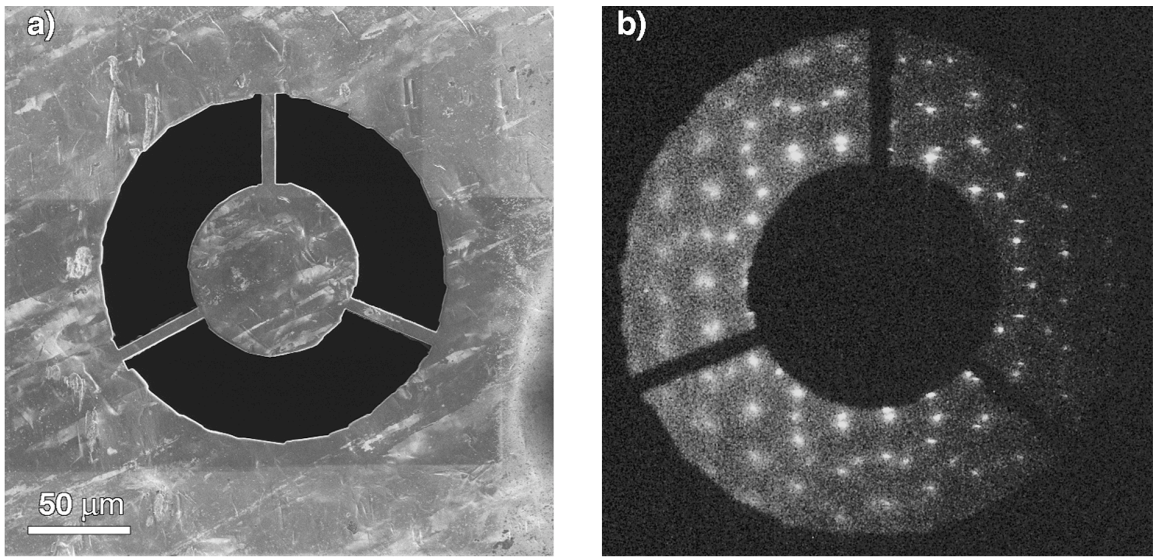

Figure 1

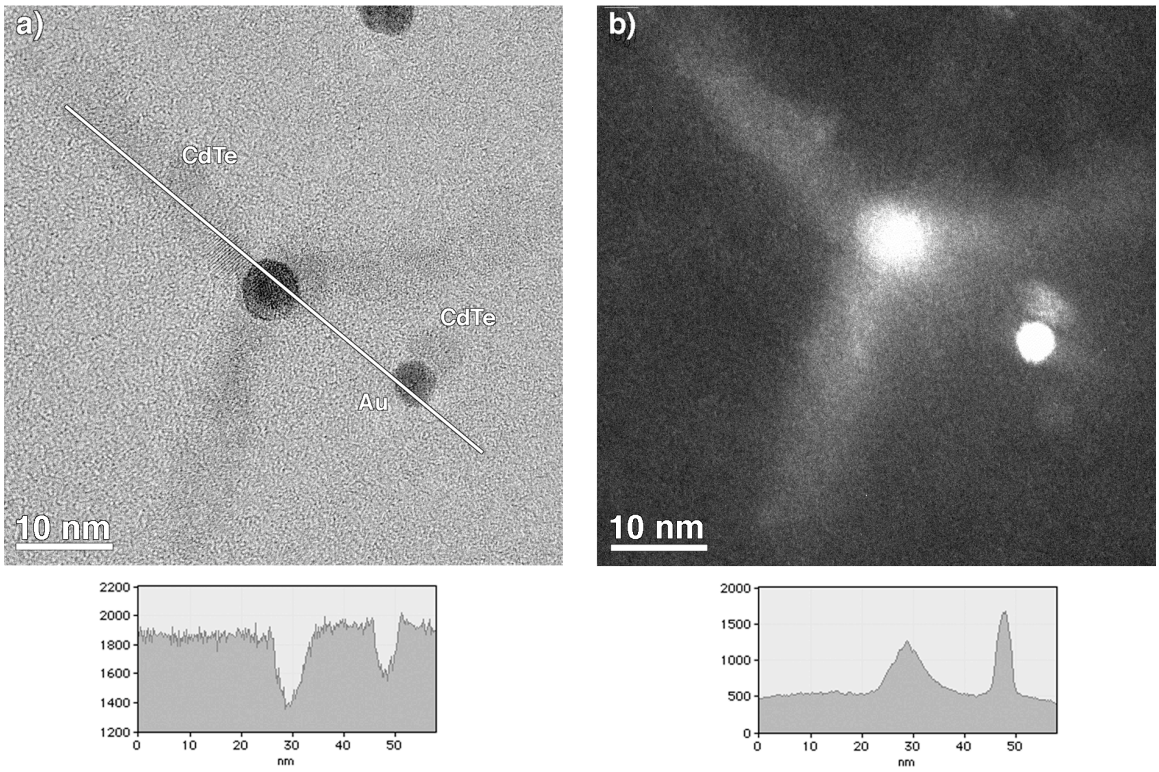
a)
CdTe
CdTe
Au
10 nm
b)
10 nm
2200
2000
1800
1600
1400
1200
0
10
20
30
40
50
nm
2000
1500
1000
500
0
0
10
20
30
40
50
nm

Figure 2

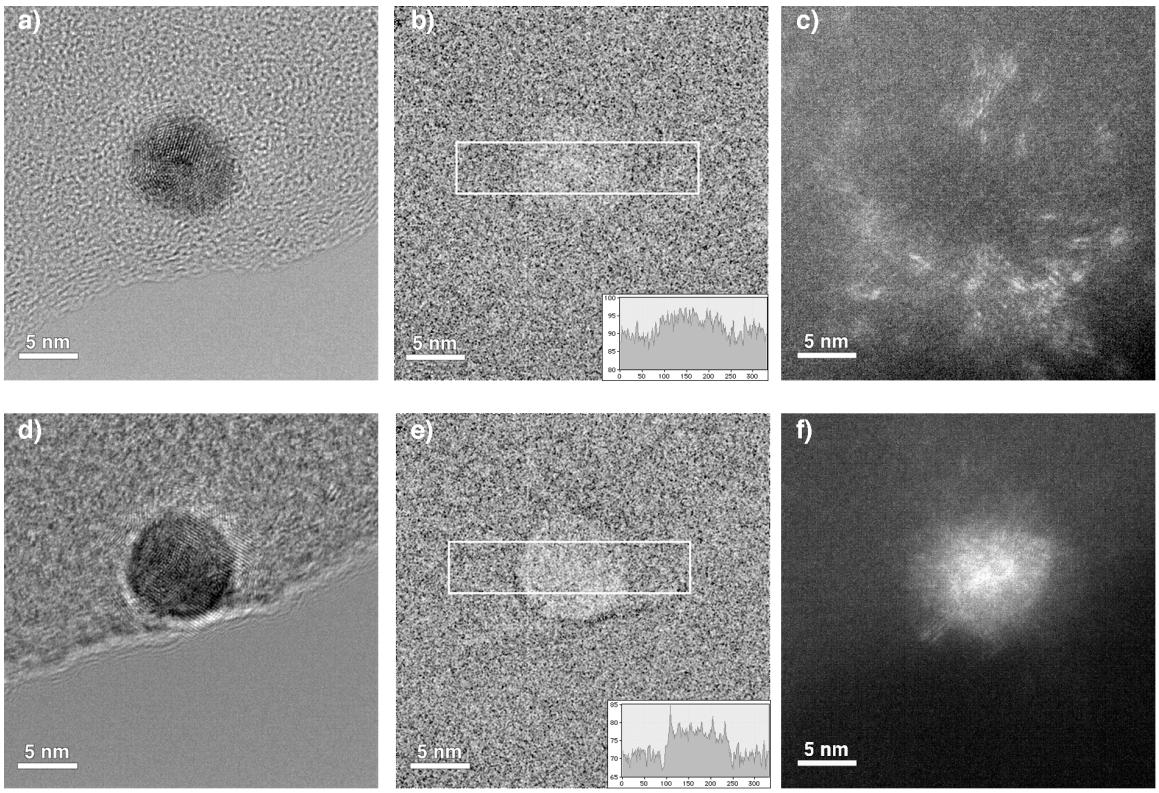

Figure 3

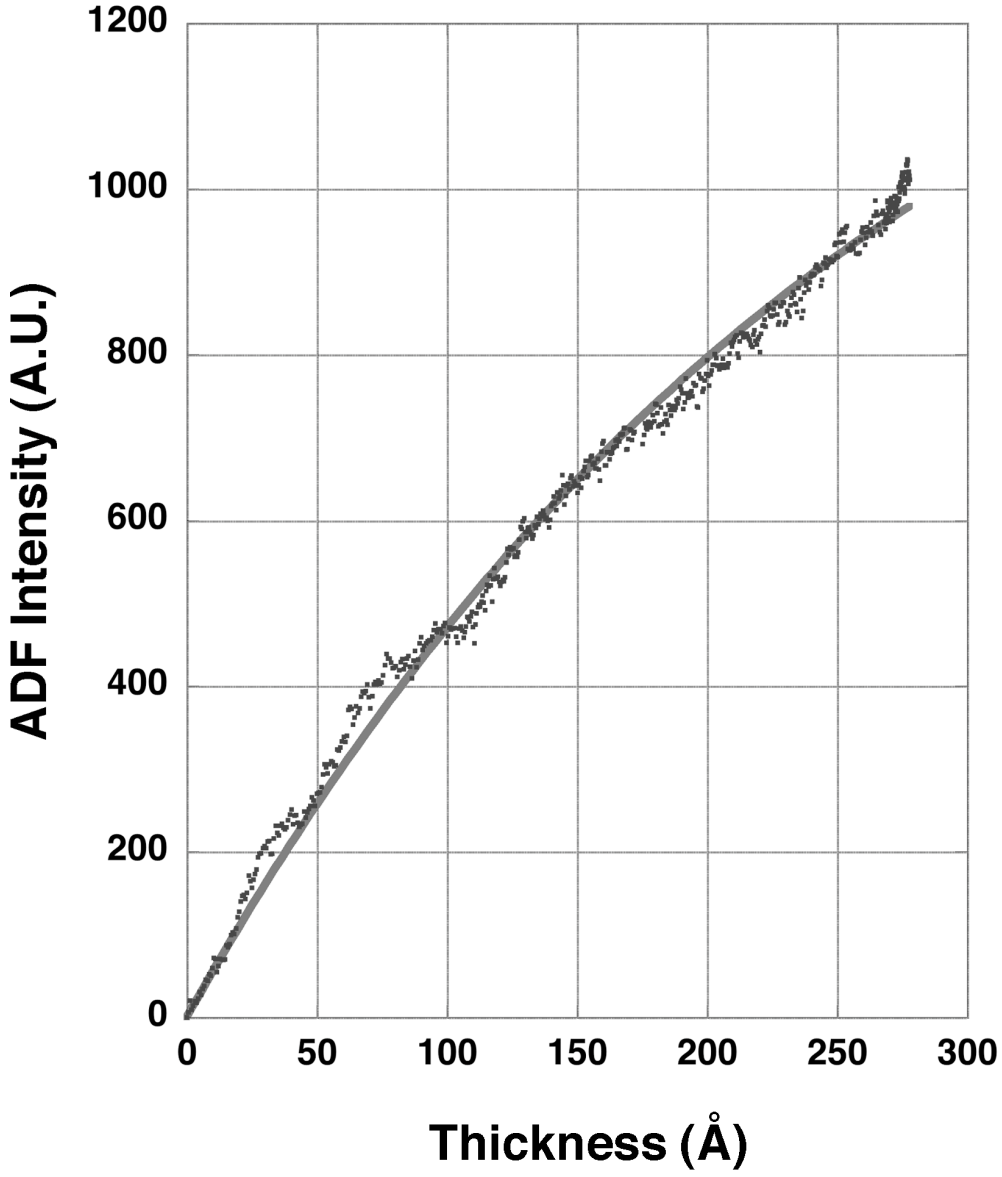
1200
1000
800
600
400
200
0
ADF Intensity (A.U.)
0
50
100
150
200
250
300
Thickness (Å)

Figure 4

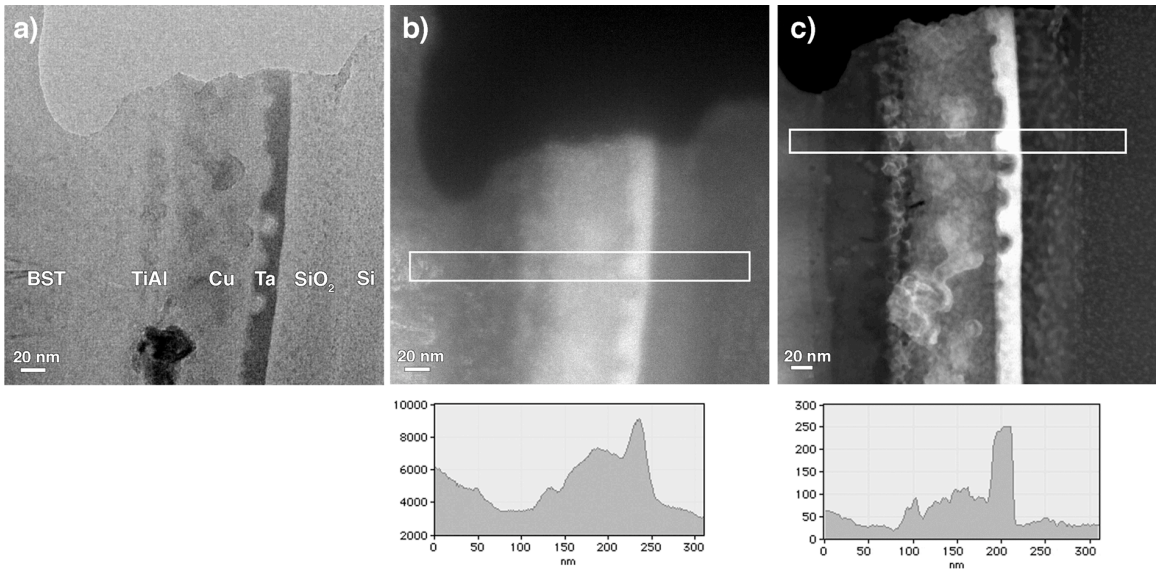
a)
BST
TiAl
Cu
Ta
SiO2
Si
20 nm
b)
20 nm
c)
20 nm
10000
8000
6000
4000
2000
0
50
100
150
200
250
300
nm
300
250
200
150
100
50
0
50
100
150
200
250
300
nm

Figure 5